Superparamagnetic and highly bioactive SPIONS/bioactive glass nanocomposite and its potential application in magnetic hyperthermia

Superparamagnetic and highly bioactive SPIONS/bioactive glass nanocomposite and its potential application in magnetic hyperthermia

*Roger Borges, Letície M. Ferreira, Carlos Rettori, Isabela M. Lourenço, Amedea Seabra, Frank Muller Emanuela Prado Ferraz, Marcia M. Marques, Marta Miola, Francesco Baino, Javier B. Mamani, Lionel F. Gamarra, Juliana Marchi**

MSc. R. Borges, Prof. L.M. Ferreira, Prof. C.Rettori, MSc. I. M. Lourenço, Prof. A. Seabra, Prof. J. Marchi
Centro de Ciencias Naturais e Humanas, Universidade Federal do ABC
Avenida dos Estados, 5001, Santo André – SP, 09210-580 Brazil,
E-mail: juliana.marchi@ufabc.edu.br

Prof. C. Rettori
Instituto de Física Gleb Wataghin, Universidade Estadual de Campinas
Rua Sérgio Buarque de Holanda, 777 - Cidade Universitária, Campinas - SP, 13083-859, Brazil

Prof. F. Muller
Institute of Materials Science, Friedrich Schiller University Jena
Löbdergraben 32, 07743 *Jena* Germany

Prof. E.P. Ferraz, Prof. M.M. Marques
Departamento de Dentística, Faculdade de Odontologia, Universidade de Sao Paulo
Av. Prof. Lineu Prestes, 2227, Cidade Universitária, São Paulo, SP, 05508-000, Brazil

Prof. M.M. Marques
Faculdade de Odontologia, Universidade Ibirapuera.
Av. Interlagos, 1329, Chácara Flora, São Paulo, SP, 04661-100, Brazil

Prof. M. Miola, Prof. F. Baino
Department of Applied Science and Technology, Politecnico di Torino,
Corso Duca degli Abruzzi, 24, Turin, 10129, Italy

Dr. Javier B. Mamani, Dr. Lionel F. Gamarra
Hospital Israelita Albert Einstein, Av. Albert Einstein, 665, São Paulo, SP 05652-000, Brazil

Keywords: bioactive glasses, iron oxide nanoparticles, superparamagnetism, bioactivity

Magnetic bioactive glass-ceramics are biomaterials aimed at being applied for magnetic hyperthermia in bone cancer treatment, thereby treating the bone tumor besides regenerating the damaged bone. However, combining high bioactivity and high saturation magnetization

still remains a challenge, since the thermal treatment step employed to grow magnetic phases is also related to loss of bioactivity. Here, it is proposed a new nanocomposite made of superparamagnetic iron oxide nanoparticles (SPIONs) dispersed in a sol-gel-derived bioactive glass matrix, which does not need any thermal treatment for crystallization of magnetic phases. The scanning electron and transmission electron microscopy, X-ray diffraction, and dynamic light scattering results confirm that the SPIONs are actually embedded in a nanosized glass matrix, thus forming a nanocomposite. Magnetic characterization evidences their superparamagnetic behavior, and the bioactivity results performed in simulated body fluid show that such nanocomposites exhibit apatite-forming properties similar to the highly bioactive parent glass (i.e., 58S composition). Finally, the calorimetric test suggests that the nanocomposites are suitable for hyperthermia applications in bone cancer treatment. The overall results evidence the obtainment of high bioactive nanocomposites with superparamagnetic properties. This methodology is a new alternative to produce magnetic bioactive materials to which the magnetic properties only relies on the quality of the SPIONs used in the synthesis. Thereby, these nanocomposites can be recognized as a new class of bioactive materials for applications in bone cancer treatment by hyperthermia.

1. Introduction

Ferromagnetic, ferrimagnetic, and superparamagnetic materials have been extensively studied for applications in the treatment of cancer by magnetic hyperthermia [1]. The basis of magnetic hyperthermia lies on the principle of applying an alternating magnetic field on a magnetic material, causing magnetic losses that are dissipated as heat, and thus increasing the local temperature. If these materials are placed next to tumors, the increase in temperature can induce weakness or death of cancer cells, still preserving the health ones [1]. It is possible because healthy cells can handle temperature stress up to 46 °C, while cancer cells handle

stress only up to 43 °C. Therefore, if the increase in temperature is precisely controlled, cancer cells are selectively killed and health ones minimally affected [2,3].

Although superparamagnetic iron oxide nanoparticles (SPIONs) are the most known materials for hyperthermia applications, there are also other ceramics with suitable magnetic properties for this purpose, such as the magnetic bioactive glass-ceramics (MBG) which have been proposed for treatment of bone cancer by hyperthermia [4]. These MBG are materials derived from the partial crystallization of bioactive glasses and are fascinating glass-ceramics due to their ability to treat bone cancer by hyperthermia while stimulating the regeneration of the bone defect caused by the tumor. The regeneration potential is due to their bioactivity, that is, their ability to form an apatite-like layer on their surface in a host tissue [5]. The bioactivity mechanism, i.e., the chemical steps involved in the formation of apatite, can be briefly divided into five stages: I) H^+ ions from the body fluid interact with Si-O-Si bonds on the glass surface, causing their cleavage by hydrolysis, and leading the formation of silanol bonds (Si-OH); II) leaching of modifier ions present in the glass structure towards the body fluid, favored by the newly formed silanol bonds; III) saturation of Ca^{2+} and PO_4^{3-} in the microenvironment of the host tissue; IV) precipitation of calcium phosphate onto the glass surface, and formation of an amorphous calcium phosphate layer; V) crystallization of the amorphous calcium phosphate into hydroxyapatite-like layer, which enables the establishment of chemical bonds between the hydroxyapatite of the bone tissue (natural mineral phase) and that grown on the glass surface [6].

Bioactivity, however, can be influenced by different factors related to the glass structure, such as the incorporation of ions in the glass network, or crystallization of the glass matrix [7] as in the case of MBG. In this sense, bioactivity and magnetization are the main issues related to MBG. According to our perspectives, the milestones in the development of MBG can be explained under the point of view of their bioactivity and magnetization, as shown in Figure 1.

The first generation of MBG is characterized by glass-ceramics with high magnetization but low dissolution and low bioactivity, as a consequence of the crystallization. It also stands for the first produced glass-ceramics in 1991 by Ebisawa et al. [8], who developed a melt-derived bioactive glass based on a $CaO\text{-}SiO_2\text{-}B_2O_3\text{-}P_2O_5$ system and doped with iron (II, III) oxide. This glass was then crystallized by thermal treatment, leading to the growth of wollastonite ($CaSiO_3$), hematite (Fe_2O_3) and magnetite (Fe_3O_4) crystalline phases. The magnetite had a crystal size of 10-120 nm and showed ferrimagnetic properties. The *in vivo* results showed the potential of these glass-ceramics to generate heat under physiologically safe frequencies and magnetic field, and their ability to osteointegrate with bone tissue [9]. However, the growth of crystalline phases during the thermal treatment arises some concerns about the chemical durability of these materials in vivo, as they could remain a long time in the host tissue and lead to undesired physiological reactions. Then, other melt-derived MBG were produced/studied in order to improve either their magnetic properties or their bioactivity [10–15].

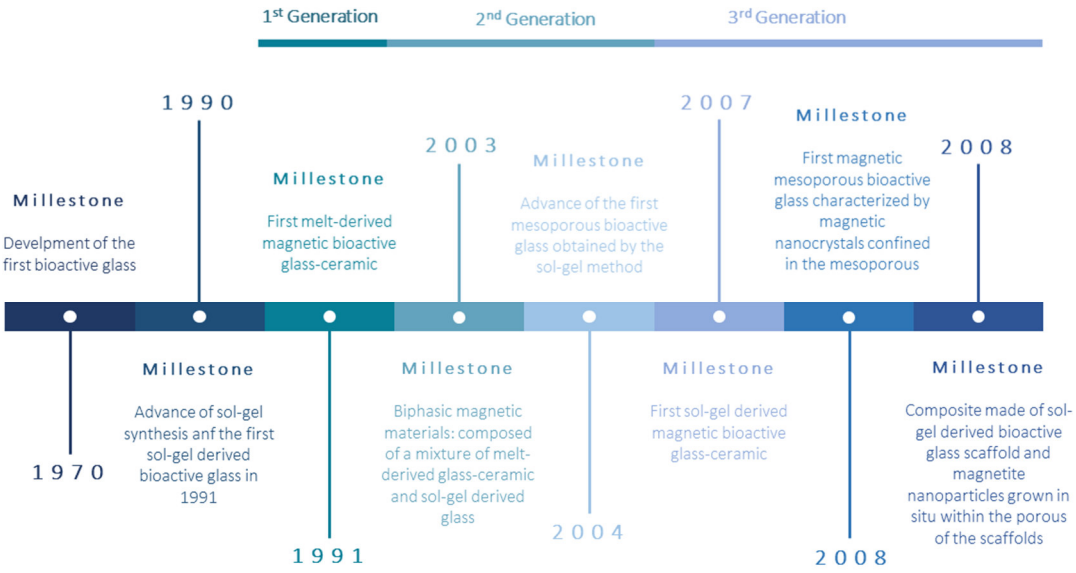

Figure 1 – Timeline of the history of MBG accoding to the authors' perspective. The different generations were based on the processing method used to obtain the magnetic phases, and ally them with bioactivity. Author's authorship.

The second generation of MBG is marked by the advance of the sol-gel synthesis of bioactive glasses between the 1990s and 2000s. These materials can be synthetized with tuned bioactivity [16,17], propitiated by the higher effective surface area and chemical reactivity of sol-gel-derived glass powders. In 2003, Arcos et al. proposed a new type of biphasic MBG [18], which were composed by a mixture of melt-derived magnetic glass-ceramic and sol-gel-derived bioactive glass (1:1 weight ratio). In this sense, these biphasic materials could ally the high bioactivity of sol-gel glasses with the magnetic properties of melt-derived glass-ceramics [18]. A couple of other works have used the same approach, but despite the improved bioactivity, the saturation magnetization (Ms) of these biphasic materials was much lower than that found in melt-derived bioactive glass-ceramics. This fact compromises the effectiveness of hyperthermia treatment. For example, while the biphasic materials showed Ms from 0.012 to 18 emu/g [18–21], purely melt-derived bioactive glass-ceramics had values of Ms between 10 and 40 emu/g [8,10–15].

In the third generation, MBG are entirely produced by the sol-gel approach. In this sense, the advent of mesoporous bioactive glasses in 2004 [22], mainly produced by the evaporation-induced self-assembly (EISA) method, provided a new technology to obtain sol-gel-derived bioactive glasses with magnetic nanocrystals grown within the walls of mesopores [23–26]. Despite the superior *in vitro* bioactivity of these materials, their magnetization still kept low, ranging from 1 to 4 emu/g, much lower than the glass-ceramics from the first generation. In 2008, Baikousi et al. [27] proposed the production of sol-gel-derived scaffolds having magnetic nanoparticles grown in the mesoporous struts, thereby forming a composite material. This composite had promising bioactive properties, evidenced by the formation of

hydroxyapatite after 3 days of immersion in simulated body fluid (SBF) solution, and they presented one of the highest magnetization (~ 7 emu/g) among sol-gel-derived materials.

This brief review of the state-of-art of MBG witnesses that to combine magnetization and bioactivity in glasses/glass-ceramics is still a challenge, mainly when these materials are processed by the sol-gel method. In this work, we proposed a new nanocomposite made of a bioactive glass matrix containing superparamagnetic iron oxide nanoparticles (SPIONs), which showed relatively high magnetization and bioactivity similar to highly bioactive glasses. The magnetic properties of the nanocomposite were tuned by using magnetic nanoparticles with improved superparamagnetic properties, contrasting with the weak magnetic properties of other MBG produced by the sol-gel method. These new glass/SPION nanocomposites are proposed as a fourth generation of highly bioactive and magnetic glass-ceramic materials.

2. Results and Discussion

2.1 – Nanocomposite structure and morphology

In this work, nanocomposites were produced based on a $58SiO_2$-$33CaO$-$9P_2O_5$ (58S) bioactive glass matrix (BG) containing different amount of synthetic SPIONs. Thus, samples were named as BGFeX (X = 10, 20 and 30), where X denotes the quantity of SPIONs (wt.%) dispersed in the glass matrix.

Initial characterization of the nanocomposites includes the identification of crystalline phases, and analysis of SPIONs dispersion in the glass matrix. Figure 2a shows the X-ray diffractograms of SPIONs, BG and BGFe compositions. While the BG powder shows a typical amorphous structure, characterized by a broad halo between 20 and 35° derived from the short-range order of silicon tetrahedrons [28], the synthetic SPIONs show a diffractogram pattern typical of magnetite nanoparticles (Fe_3O_4, ICDD 1-075-1609) [29]. On the other hand, the BGFe nanocomposites exhibit X-ray diffraction features from both the glassy and the crystalline phases, that is, peaks related to magnetite and a broad halo over 20 and 35°. The

amorphous character of the nanocomposites is prominent in those containing lower quantities of SPIONs, while the peaks related to magnetite phase are more eminent in those containing a higher fraction of nanoparticles. In addition, the X-ray results highlight a peak at 14° in the BGFe10 composition, which may be attributed to the formation of secondary calcite phase ($CaCO_3$, ICDD 1-086-2334) along with the synthesis. The formation of calcite residues is typically found in the sol-gel synthesis of bioactive glasses, mainly those in the 58S system [30,31], and are nucleated on the glass surface. Usually, these crystals can act as apatite precursors, thus also improving bioactivity [32]. Their development is not associated to glass devitrification derived from thermal treatments which may jeopardize bioactivity; detailed explanation concerning the calcite formation mechanism can be found in refs [30,31]. Being nucleated on the glass surface, this phase does not change the glass structure like a crystallization from thermal treatments. This fact can be considered as an advantage, since most of the glass-ceramics from the First and Second Generation, as well as some from the Third Generation, often show massive growth of undesired crystals during the thermal treatment. The main problem of undesired crystallization is the loss of bioactivity in glass-ceramics containing more than 30 wt.% of a crystalline fraction [7], besides diminishing of zeta potential in the glass surface, which decreases the absorption of proteins involved in the adhesion, proliferation, and differentiation of cells from bone tissue [33]. Our proposed nanocomposites were synthetized through an innovative methodology, which did not lead to the formation of any undesired phases, other than calcite, because it is based on the formation of a glass network surrounding the magnetic nanoparticles. Besides, our materials were calcinated at 550 °C, which is a suitable temperature to promote the inclusion of glass network modifiers in the glass network as well as to calcinate residues from the synthesis process [34,35], but lower enough to avoid crystallization of the glass structure.

Figures 2b-d shows the dynamic light scattering (DLS) results from the BG glass and the BGFe nanocomposites. The proposed synthesis yields the production of nanometric

materials, which have a particle size distribution between 100 and 1000 nm, as noted in the BGFe10 (534 ± 62 nm), BGFe20 (374 ± 24 nm) and BGFe30 (604 ± 59 nm) nanocomposites. However, the nanocomposites contrast with their parent BG glass, which showed bigger particles (1550 nm ± 120 nm). Considering the difference between particle growth in the presence or absence of SPIONs, we propose a growth mechanism, as illustrated in Figure 2f.

In the absence of SPIONs (upper illustration, Fig. 2f) the glass formation mechanism occurs like proposed by Lin et al. [35], which is composed by three stages: i) condensation: in this stage, there is the formation of Si-O-Si and eventual P-O-Si bonds through polycondensation reactions during the sol-gel transition, which causes the formation of primary particles; ii) drying: this stage happens during drying of the obtained gel, which leads to primary particle agglomeration (formation of secondary particles), and precipitation of calcium nitrate onto the secondary particles; iii) stabilization: the last stage occurs after calcination, where the nitrates are thermally decomposed, and calcium ions are incorporated in the secondary particles as glass modifiers, also promoting the fusion of secondary particles, thereby forming tertiary particles.

In the presence of SPIONs (lower illustration, Fig. 2f), however, primary particles (stage i) are formed by heterogeneous nucleation of the gelly phase during the sol-gel transition. Due to the presence of many SPIONs in the synthesis, there are many nucleation sites that allow the formation of smaller primary particles. As a result, after stages (ii) and (iii), the final particle size is smaller than that of the glasses obtained in the absence of SPIONs.

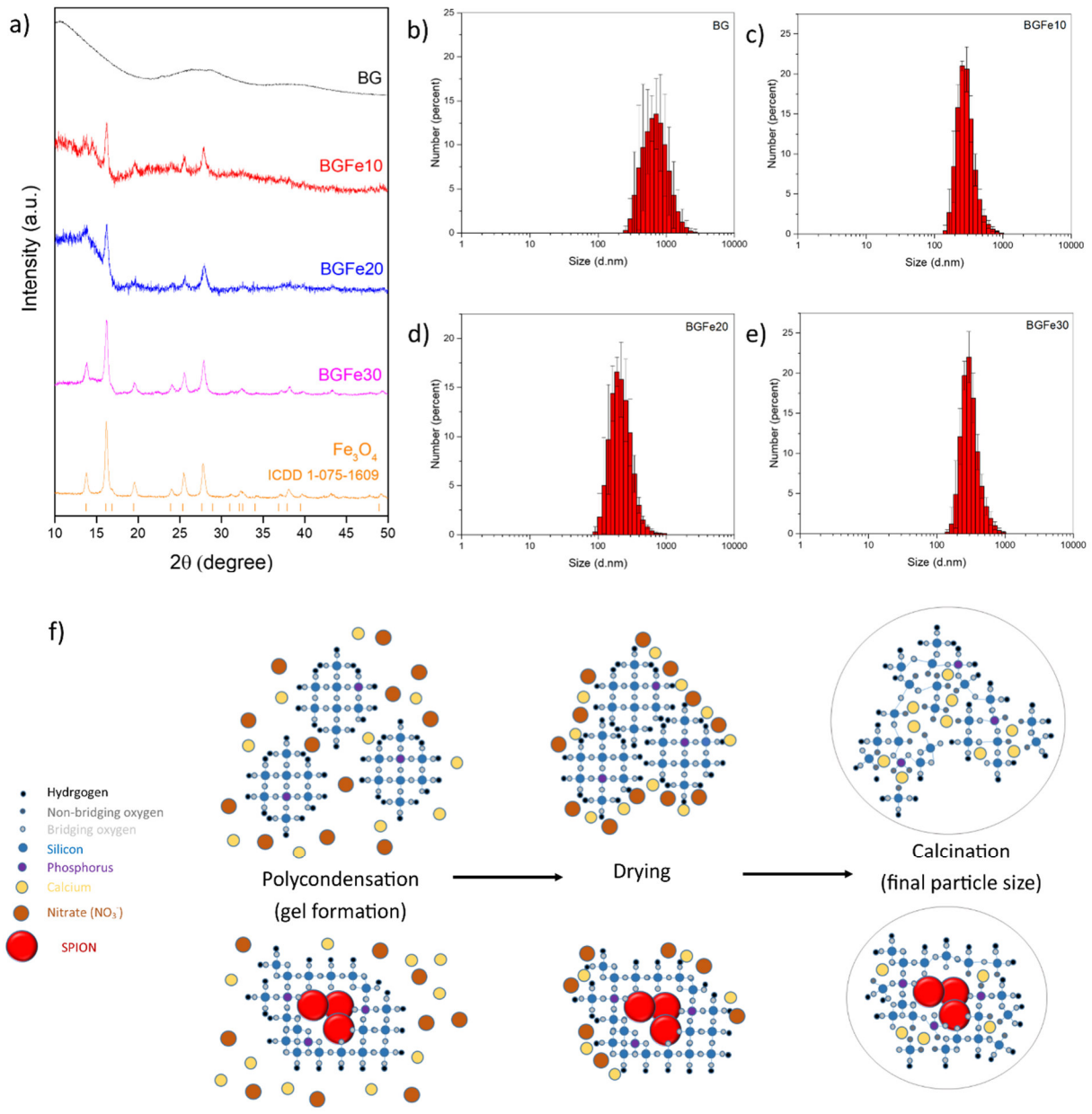

Figure 2 – Structural characterization of BGFe nanocomposites: a) XRD diffraction pattern of the nanocomposites in comparison with SPIONs, ICDD 1-075-1609 (Fe_3O_4) and BG. (b-e): Particle size measurements by DLS: b) BG; c) BGFe10; d) BGFe20; e) BGFe30. f) Scheme of the glassy phase formation in the absence (upper images) or presence (lower images) of SPIONs. The illustration was based on the mechanism proposed by Lin et al. [35] and adapted by the authors for the synthesis performed in the presence of SPIONs.

The micrographs of the nanocomposites further confirmed the proposed mechanism of particle growth in the presence of SPIONs. Figure 3a-b shows representative FEG-SEM images of the BG glass and the BGFe10 nanocomposite, respectively. Briefly, it is observed that the materials are composed of agglomerated nanoparticles, which agrees with the observed DLS results. Nanosized particles was expected since the synthesis was based on the quick-alkali method [34]. Figure 3c-d shows representative FEG-SEM and TEM micrography of the BGFe30 composition. At higher FEG-SEM magnification (Fig. 3c), it is possible to observe the formation of tertiary particles derived from secondary ones due to coalescence occurred during the calcination process. Also, the TEM image (Fig. 3d) shows that the SPIONs are embedded in the glass matrix. However, EDS analysis of glass particles (Figures 3e-i) suggests that the SPIONs may not be homogeneously dispersed in the glass matrix. Figure 3i shows the EDS mapping of iron dispersed in the glass matrix. Some nanocomposite particles are more abundant in SPIONs than others, which suggest that SPION clusters are present in the glass matrix.

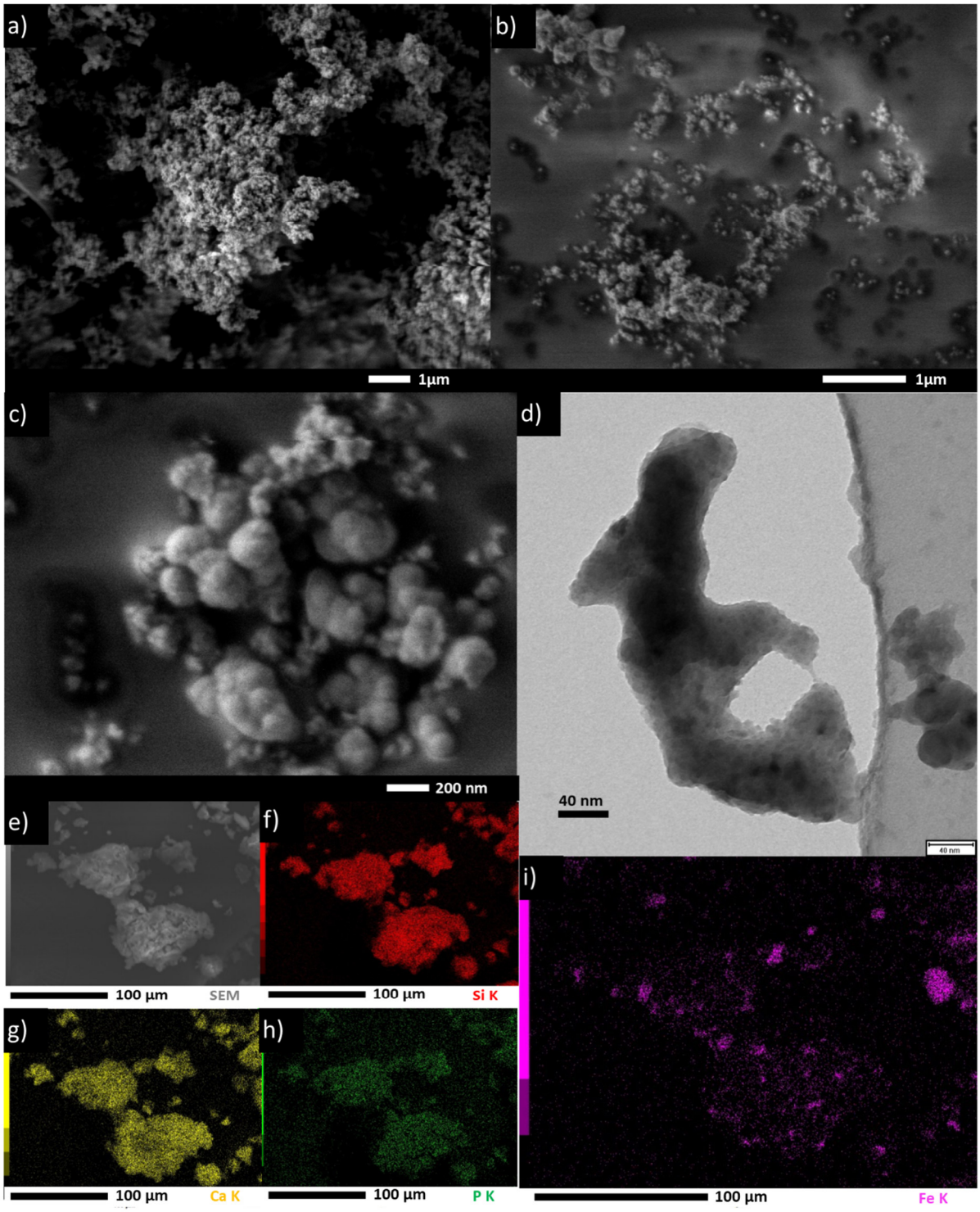

Figure 3 – Morphological characterization of the nanocomposites: a) FEG-SEM micrograph of BG glass; b) FEG-SEM micrograph of the BGFe10 nanocomposite; c) FEG-SEM (at higher magnification) of the BGFe30 nanocomposite; d) TEM micrography of the BGFe30 nanocomposite. (e-i) Compositional mapping obtained by SEM-EDS analysis of the BGFe20

nanocomposite: e) SEM image; f) silicon mapping; g) calcium mapping; h) phosphorus mapping; i) iron mapping

2.2. Magnetic characterization

Superparamagnetic particles are usually characterized by the absence of hysteresis in M-H graphs (magnetization in the function of a magnetic field), and by the presence of blocking temperature (T_B) in ZFC-FC curves (zero-field cooling field-cooling) (BIHLMAYER, 2007; CANNAS et al., 2001; YANG et al., 2005; MANDEL et al., 2013). The nanocomposites are expected to show a superparamagnetic behavior due to SPION incorporation. The M-H curves of BGFe compositions are shown in Figure 4a. The BG glass showed an M-H curve typical of a paramagnetic material, which contrasts with the sigmodal shaped curve characteristic of superparamagnetic materials found in the BGFe nanocomposites. The absence of hysteresis in the BGFe nanocomposites is better observed in the insert of Figure 4a, which indicated that the measurements were carried out above the blocking temperature of the nanoparticles, since coercitivity and remanent magnetization are only observed below the blocking temperature. The saturation magnetization (M_s) of the nanocomposites was 5.7, 8.9, and 15.1 emu/g for the BGFe10, BGFe20, and BGFe30, respectively. As expected, the values of M_s increase with the addition of SPIONs in the glass matrix, since the density of magnetic domains in the resulting nanocomposite increases.

In the ZFC curve of superparamagnetic materials, its maximum ($\delta M/\delta T = 0$) represents the mean blocking temperature (T_B), that is, the average temperature where the mean magnetic particle size has a magnetic fluctuation of their spins. The temperature in which the FC curve meets ZFC one is assumed as the irreversible temperature (T_{irr}), the temperature in which the biggest particle has its spins magnetically fluctuating [39]. The difference between T_B and T_{irr} can be related to the distribution of magnetic particle size.

However, it is common to observe T_B and T_{irr} occurring at the same temperature, which is associated with uniform magnetic particle size distribution. Furthermore, T_B is also directly associated with the magnetic interactions between magnetic particles. Usually, magnetic interactions are due to dipole-dipole or exchange interactions, but when the magnetic particles are embedded in a diamagnetic matrix, such as our bioactive glasses, only dipole-dipole interactions are possible [2,37–39].

Figure 4b shows the ZFC-FC curves of our BGFe nanocomposites. The values of T_B for the BGFe10, BGFe20 and BGFe30 compositions were 116, 102, and 96 K, respectively. These values are higher than that of the SPIONs used in this work (72 K, see reference [40]). This fact highlights the presence of dipole-dipole interactions between the nanoparticles. Thus, the systematic decrement of T_B from the BGFe30 to BGFe10 indicates that the BGFe10 composition shows more dipole-dipole interactions than the BGFe30. According to Mendel et al. [39], this effect of dipole-dipole interactions is more substantial when the SPION clusters become more prominent, which implies that the BGFe10 has more massive SPION clusters than the BGFe30 (see the illustration of this phenomena in Figure 4e).

Moreover, the peak shape of the ZFC curve also contributes to new information about dipole-dipole interactions. Figure 4c shows the peaks of the ZFC curves intentionally overlapped. Nanocomposites containing a higher fraction of SPIONs present sharpy features, while a broader peak is observed in those compositions with fewer SPIONs. Usually, this phenomenon is also associated with magnetic interactions between particles, where broader peaks are related to more intense dipole-dipole interactions [2,37–39]. This fact is in agreement with the analysis of blocking temperature aforementioned and supports the presence of dipole-dipole interactions.

The previous observation about the size of SPION clusters in the different nanocomposites – deriving from the analysis of T_B – is in perfect agreement with the mechanism reported by Deng et al. [41], who suggested that the TEOS/SPION ratio used in the

synthesis process influences the formation of magnetic clusters. In this sense, the lower TEOS/SPION ratio leads to smaller SPION clusters in a glass matrix. In our experiments, we used TEOS (tetraethyl orthosilicate) as silicon source for the glass synthesis. The TEOS/SPION ratio was 19, 8, and 5 for the BGFe10, BGFe20, and BGFe30 compositions, respectively, which justifies our results that indicate the BGFe30 composition as having smaller (i.e. less massive) SPION clusters.

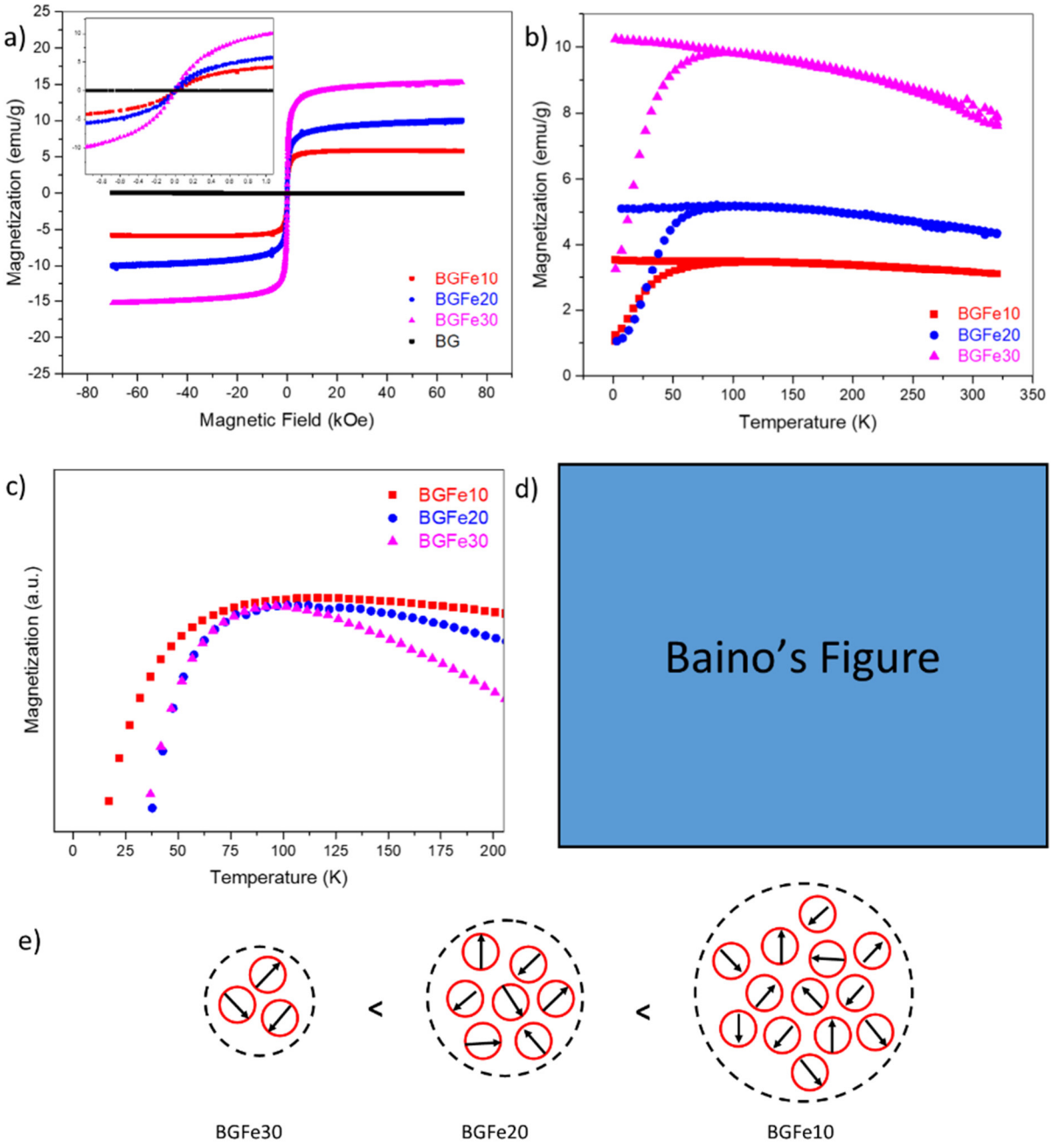

Figure 4 – Magnetic characterization of the nanocomposites: a) M-H curves; b) ZFC-FC curves; c) ZFCs curves intentionally overlapped for better visualization of their broadening; d) calorimetric test; e) representative illustration about SPION cluster size in the different BGFe nanocomposites.

Figure 4d shows the temperature increase (ΔT) of nanocomposites; the trend is almost linear for all the formulations, as demonstrated by the high values of R^2 following a linear interpolation. The reached temperatures after 8-10 minutes of magnetic induction demonstrated that the nanocomposites are potentially suitable for hyperthermia applications: in fact, a temperature of 41-43 °C (starting from a body temperature of 37 °C) is enough to selectively kill cancer cells [ref]. The temperatures increase with the amount of SPIONs introduced in the glasses; however, only a slight difference was noticed between BGFe20 and BGFe30 samples. SPION-associated heating depends on the specific absorption rate (SAR), which was shown to decrease with increasing aggregate size of magnetic nanoparticles [ref]: this is consistent with the results from calorimetric tests and magnetization characterization.

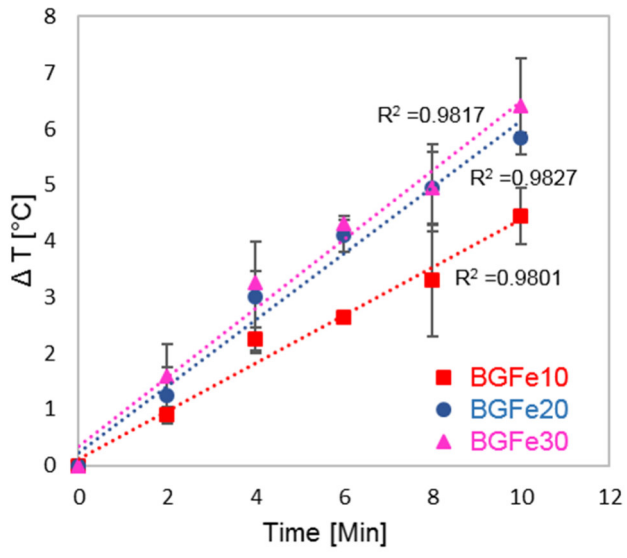

Figure 4e

2.3 Bioactivity evaluation of the nanocomposites

Bioactive materials are those which exhibit an apatite-forming ability when immersed in the body fluid [6,42,43]. Therefore, the discussion henceforth will focus on the evaluation of apatite presence on the BGFe nanocomposite surface after immersion in the SBF solution.

The XRD results of BG glass and the BGFe nanocomposites before and after immersion in the SBF solution for 1 and 7 days are shown in Figure 5 (left column). As the composites were kept in the SBF solution, diffraction peaks at 26° and 32° becomes evident, which are typical of the (004) and (002) planes from crystalline apatite phases like hydroxyapatite [44]. These peaks become more intense from the first day to the seventh day of immersion in SBF solution, which suggests not only the formation of an apatite crystalline phase but also its growth with time. These results give valuable evidence about the nanocomposite bioactivity. The calcite phase found on the surface of the BGFe nanocomposites (see section 2.1) was not observed after immersion in SBF solution, which suggests its dissolution and reprecipitation as an apatite phase.

In the BG glass, there is also the formation of calcite ($CaCO_3$, ICDD 1-086-2334), but after seven days of immersion in the SBF solution. This calcite has a different origin from that found in the BGFe10 nanocomposite (Figure 2a) before immersion in SBF. The calcite observed in the BG glass is a consequence of interactions between carbonate ions from the SBF solution and calcium ions leached from the glass particles [32]. The formation of calcite is favored in contrast to hydroxyapatite when the calcium release is too high. Usually, the hydroxyapatite is later favored when the calcium concentration is lowered due to partial consumption for the formation of calcite. However, this calcite can dissolve with time and reprecipitate as hydroxyapatite, as observed in the results of the nanocomposites. Furthermore,

calcite is also used as a biomaterial for bone regeneration, and its formation along with bioactivity test does not jeopardize the glass bioactivity [32].

The FTIR analysis (Figure 5 middle and right columns) also contributed to even more interesting findings about the nature of the calcium phosphate deposited on the materials surface. Overall, all the samples show the following functional groups: $P{=}O_{cryst.}$ (565 and 605 cm^{-1}), $P{=}O_{amorph}$ (585 cm^{-1}), SiO_2 structural (800 cm^{-1}), Q^0 (875 cm^{-1}), Si-OH (956 cm^{-1}), PO_3^{2-} (1030 cm^{-1}), Si-O- (1063 cm^{-1}), P=O (1100 cm^{-1}), Q^3 (1135 cm^{-1}) and Q^4 (1200 cm^{-1}) [45–47]. Among these functional groups, some of them are part of the glass structure like SiO_2 structural, Q^0, Si-OH, Si-O-, Q^3 and Q^4, while the groups $P{=}O_{cryst.}$, $P{=}O_{amorph}$, PO_3^{2-} e P=O come from either the glass structure or the calcium phosphate deposited on the surface of the materials.

The notations Q^0, Q^3, and Q^4 refer to silicon tetrahedron units, where the uppercase number indicates the number of bridging oxygens bonded to the silicon tetrahedrons [48,49]. The Si-OH bonds are residual of glass synthesis or may come from interactions between Si-O-Si bonds and water molecules, leading to the formation of silanol bonds [50]. The functional group Si-O- is associated with non-bridging oxygen bonds. The SiO_2 structural bond is due to the breathing of silicon tetrahedron in its transversal section [45]. In general, either the BG glass or the BGFe nanocomposites show these functional groups before immersion in the SBF solution.

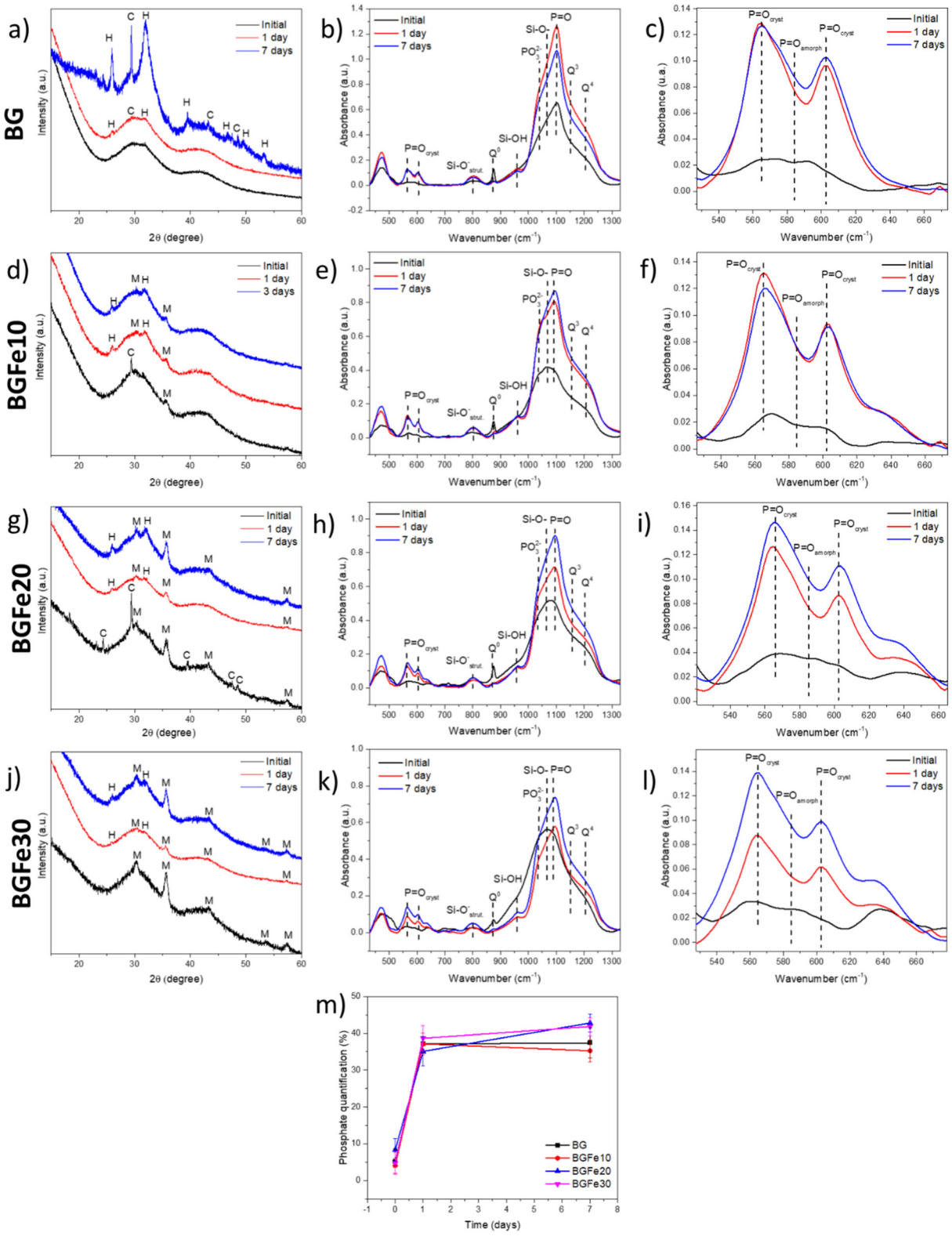

Figure 5 – Analysis of BG glass and the BGFe nanocomposite surfaces before and after soaking in SBF solution for 1 and 7 days. Left colum: XRD results of BG (a), BGFe10 (d), BGFe20 (g) and BGFe30 (j). Middle column: FTIR analysis of BG (b), BGFe10 (e), BGFe20 (h) and BGFe30 (k). Right columns: FTIR analysis (in a zoom range) of the phosphate

functional groups of BG (c), BGFe10 (f), BGFe20 (i) and BGFe30 (l). m) Phosphate quantification derived from phosphate functional groups analysis.

The PO_3^{2-} and P=O functional groups are present in either amorphous or crystalline phosphates compounds, but the $P{=}O_{cryst.}$ and $P{=}O_{amorph}$ bonds are specific of crystalline and amorphous phosphate compounds, respectively. Thereby, these last two functional groups identify the nature of the calcium phosphate layer formed on the materials surface and were analysed complementarily to the XRD results. Right columns of Figure 5 show the zoom of the wavenumber region convering $P{=}O_{cryst.}$ and $P{=}O_{amorph}$ bonds of the BGFe compositions.

Regarding the BG glass, before immersion in SBF (Figure 5b) there is a more intense peak of Si-O- which is related to the high concentration of non-bridging oxygens from the glass structure. Upon soaking the glasses in the SBF solution, however, there is a displacement of this peak towards the P=O functional group, suggesting a calcium phosphate deposition on the glass surface. This behavior agrees with the SEM results. Furthermore, it is noted that initially the calcium phosphate was centered in the $P{=}O_{amorph}$ bond, still overlapped with $P{=}O_{cryst}$ ones (Figure 5c). However, after one day of immersion in the SBF solution, a well-defined splitting of this peak was observed, which is related to a higher concentration of $P{=}O_{cryst}$ bonds, also evidencing the formation of crystalline apatite phases on glass surfaces, in good agreement with the XRD results.

Very similar behavior was found in the BGFe nanocomposites (Figures 5e-f, 5g-i and 5k-l), which suggests no difference in bioactivity behavior between the BG glass and the BGFe nanocomposite series. In addition, Figure 5m shows the phosphate quantification of the samples before and after soaking in SBF solution, using a methodology approached by FTIR data [44]. Before being immersed in SBF, the materials have phosphate content around 9 wt.% which is very close to the nominal amount of P_2O_5 in the glass compositions. After immersion, the materials surfaces become reacher in phosphate, yielding nearly 40 wt.% of phosphate,

indicating a massive formation of hydroxyapatite. Moreover, these results highlight that the amount of crystalline apatite formed on the BGFe nanocomposite surface is very similar to that found in the BG glass, which is a highly bioactive composition.

Qualitative SEM-EDS results of compositional mapping (Figure 6) show the calcium phosphate deposition on glass and BGFe nanocomposite surfaces after soaking in SBF solution. For all the studied materials, there is an increase in yellow and green intensity, just after one day of immersion in the SBF solution, which is associated with deposition of calcium and phosphate species, respectively. The same trend is observed for further soaking of the materials in the SBF solution for 7 days. Also, as they stay immersed in the SBF solution, there is a gradual decrement in red intensity, which is associated with a progressive replacement of silicon at the surface by a calcium phosphate-rich layer. In addition, the SPION cluster behavior is still observed upon soaking in the SBF solution, which suggests that the nanoparticles kept embedded in the glass matrix.

Dr. Emanuela and Dr. Marcia, please insert your results here. Discussion will be performed focusing on the effect of SPIONs fraction on the cytotoxicity and osteogenic differentiation.

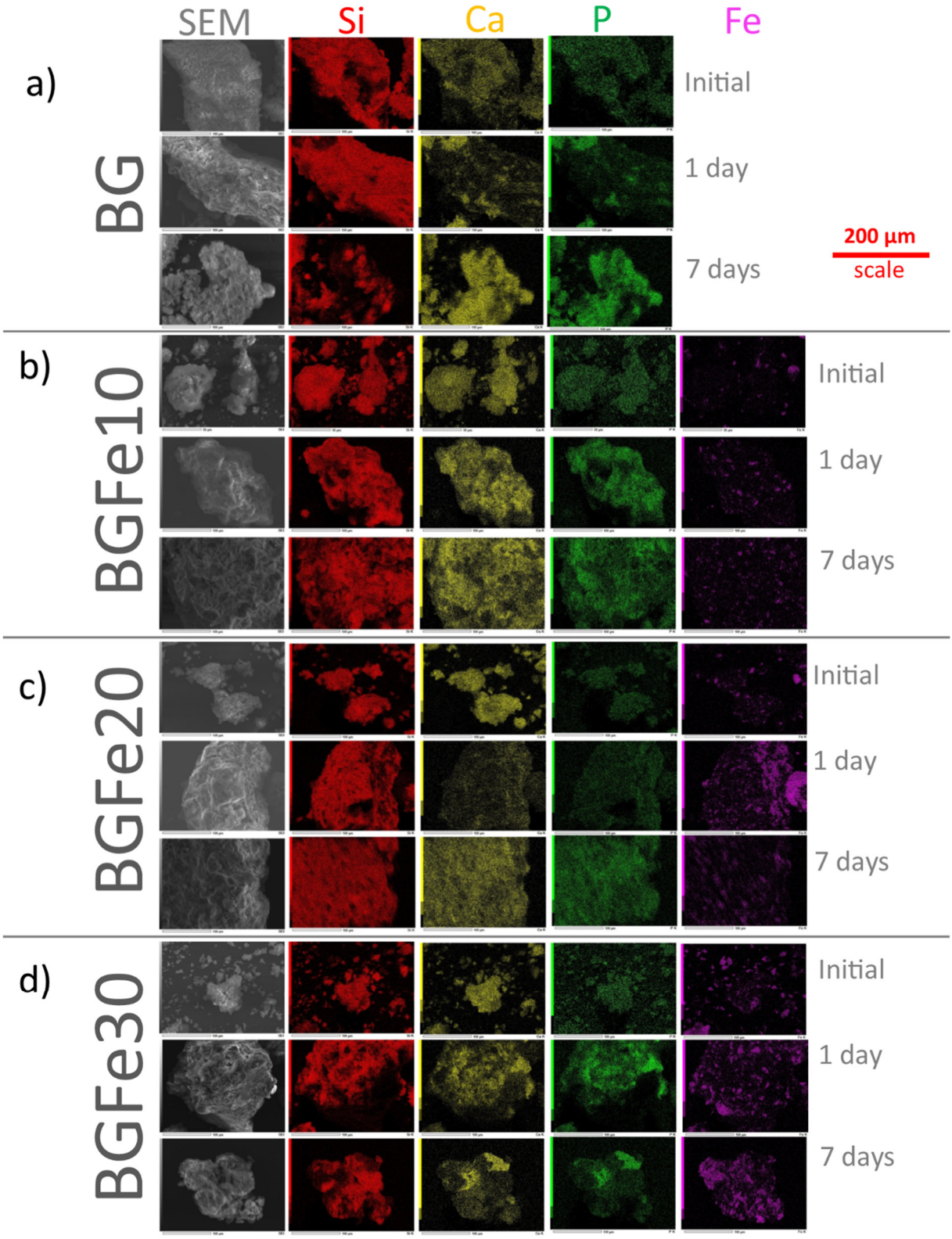

Figure 6 – SEM-EDS analysis of the studied materials before and after soaking in SBF solution for 1 and 7 days: a) BG; b) BGFe10; c) BGFe20; d) and BGFe30.

2.3 A hope for the 4th generation of MBG

As pointed out in the introduction section, the different generations of MBG were able to significantly improve the glass-ceramic magnetization or bioactivity, but not both properties simultaneously. One of the main problems of such materials was the need for thermal treatments that led to the growth of undesired phases or to structural changes that display influence on bioactivity. In this work, we were able to: i) improve magnetization of sol-gel-derived MBG; and ii) produce a highly bioactive nanocomposite.

A Ashby diagram is proposed in Figure 7a, which correlates the fraction of magnetic phase in the glass structure with the saturation magnetization, as an exciting indicator of the effective magnetization of the samples. The saturation magnetization is expected to increase as more magnetic phases is added into the glass structure, which is a consequence of more virtual magnetic domains available in the materials. However, this behavior is not systematically noted because the thermal treatments carried out in the ceramics reported in the literature did not lead to efficient conversion of magnetic ions into magnetic crystalline phases, like maghemite, magnetite or ferrites. Our BGFe nanocomposites, however, show a linear saturation magnetization trend, because the magnetic properties do not rely on the synthesis process but on the quality of the SPIONs used instead. In this sense, it was possible to achieve magnetic properties similar to those of melt-derived glass-ceramics, even though we used the sol-gel approach. For example, the sample BGFe30 showed a saturation magnetization of 15.1 emu/g, while the highest value reported in the literature is 32 emu/g [9], which is derived from ferrimagnetic crystals that have inherent higher magnetization than superparamagnetic phases. When the Ms of our nanocomposites is compared with other sol-gel-derived MBG, which ranges from 0.1 and 7 emu/g, the results obtained here are much more satisfactory.

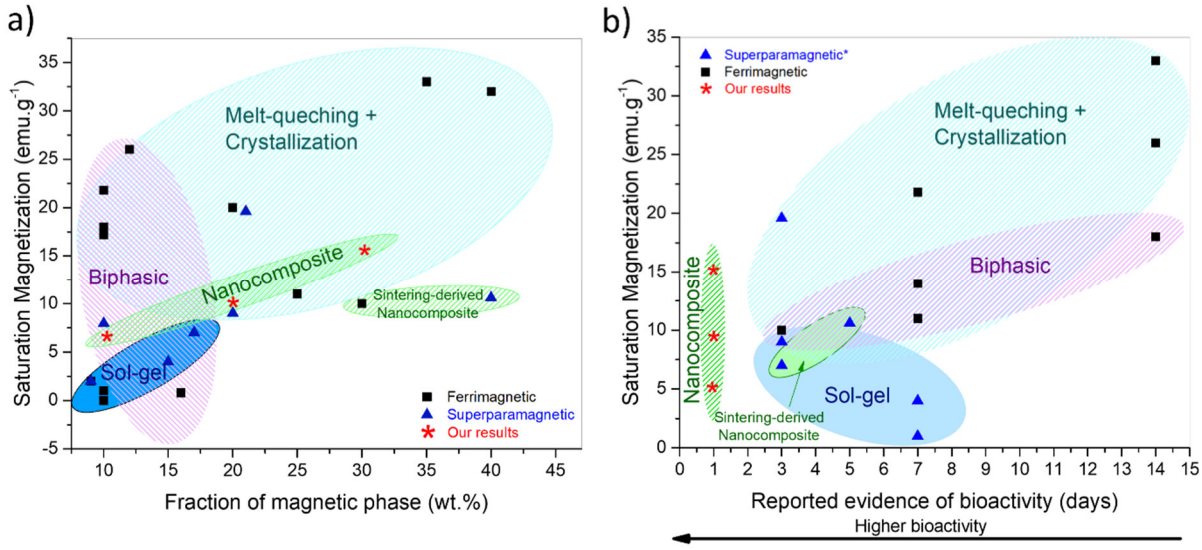

Figure 7 – Ashby diagrams based on the results from MBG found in the literature. The materials were classified into ferrimagnetic (black squares) or superparamagnetic (blue triangle). Our results are presented as red star. In another classification, the materials were grouped into melt-quenching + crystallization (analogous to 1st. Genetation of MBG) [9,11–15,51,52], biphasic (analogous to 2nd. Genetarion of MBG) [18–21], sol-gel and sintering-derived nanocomposites (both analogous to 3rd. Generation of MBG) [24,25,27,53–57]. Left image (a) correlate the fraction of magnetic phase with saturation magnetization. Right image (b) correlate the reported evidence of bioactivity with saturation magnetization.

Another interesting issue is that the addition of SPIONs in the glass matrix does not jeopardize their bioactivity, and all the studied BGFe nanocomposites showed similar calcium phosphate deposition like the parent highly bioactive 58S glass. The diagram in Figure 7b shows the correlation between saturation magnetization of MBG and their bioactivity. We assumed the first observation of calcium phosphate deposition on MBG surface upon soaking in SBF solution as the evidence of bioactivity. Considering that not all the researchers followed the same protocol or did not perform their bioactivity tests in the same periods, data presented on Figure 7b may be biased. However, to the best of the authors' knowledge, it was

the very first time that a MBG showed bioactivity within 1 day immersed in the SBF solution. We believe that MBG derived from thermal treatment, like those reported in the literature, have structural changes caused by the addition of iron in the glass structure, which alters glass dissolution and bioactivity. When we added SPIONs in the glass matrix, on the other hand, we did not change the glass structure, which remained very suitable for a highly bioactive performance of the material. Special attention should be given to highly bioactive ceramics because the apatite-forming ability directly reflects on the osteointegration properties of bioceramics. The establishment of chemical bonds between the apatite formed on the bioceramic surface and the "natural" one found in the host tissue avoids the formation of scar tissue that could jeopardize the bone regeneration, and its consequent osteointegration, which is one of the three pillars of bone regenerations, together with osteoconductivity and osteoinduction [58].

Taken all these points together, the new BGFe nanocomposites proposed here offer a new solution for the development of highly magnetic and bioactive MBG and may stand as the fourth generation of MBG.

3. Conclusion

Superparamagnetic and highly bioactive nanocomposites made of SPIONs dispersed in a bioactive glass matrix were successfully obtained through the sol-gel method. The structural characterization performed by XRD, SEM, and EDS confirmed the nanoscale nature of the nanocomposite and showed that SPION clusters were dispersed in a glass matrix. Besides, the superparamagnetic behavior of the nanocomposites was evidenced by magnetic characterization, and the blocking temperature showed to be affected by the SPION clusters. Magnetization characterization revealed that the SPION clusters were larger (i.e. more massive) in those nanocomposites containing a lower fraction of SPIONs. The saturation

magnetization of these nanocomposites was as high as those found in magnetic bioactive glass-ceramics obtained by melt-derived techniques with ferrimagnetic properties, which are inherently more magnetic than superparamagnetic materials. All the BGFe nanocomposites showed high bioactivity, which was compared with that of a 58S bioactive glass, a highly bioactive sol-gel derived glass. Also, the bioactivity was independent of the fraction of SPIONs embedded in the glass matrix. Therefore, these nanocomposites combine high saturation magnetization and high bioactivity, overcoming the challenge of co-existing both in the same material. Thus, they stand as a possible new class of superparamagnetic bioceramics that can be potentially applied for the treatment of bone cancer by magnetic hyperthermia.

4. Experimental Section

Glass and Nanocomposite Synthesis: In this study, four compositions were studied: BG, BGFe10, BGFe20, and BGFe30. The BG glass is based on the 58S bioactive glass composition ($58SiO_2$-$33CaO$-$9P_2O_5$, values in wt.%). The nanocomposites have their matrix composition like the 58S bioactive glasses, but have different incorporation of synthetic SPIONs in their structure: 10 wt.% (BGFe10), 20 wt.% (BGFe20) and 30 wt.% (BGFe30).

The BG glass synthesis was based on the quick-alkali method [34] and adapted by our research group [59,60], which aims to produce bioactive glass nanoparticles. In brief, tetraethylorthosilicate (TEOS) and triethyl phosphate (TEP) were hydrolyzed in a solution containing water, ethanol, and nitric acid (1 M). After stirring by 20 min, calcium nitrate tetrahydrate was added and the batch was stirred for more than 20 min. Then, ammonia solution (2 M) was quickly dropped into the acid solution to induce the sol-gel transition. After this last step, the resulted gel was dried by freeze-drying (Operon, South Korea) for 24 h and then calcinated at 550 °C/1 h in an electrically-heated furnace (EDG 300, Brazil).

For the production of the nanocomposites, synthetic SPIONs were added in the synthesis process together with calcium nitrate tetrahydrate. All the other steps were carried out similarly as glass nanoparticles, except for the calcination, which was carried out in a tubular furnace (Lindberg Blue M, USA) under argon atmosphere to avoid SPIONs oxidation. The SPIONs were previously synthesized and characterized by the research group, as described in [40].

Structural Characterization: The glass and nanocomposites were characterized regarding their structure by X-ray diffraction (XRD), dynamic light scattering (DLS), field-emission scanning electron microscopy (FEG-SEM), scanning electron microscopy coupled with energy dispersive spectroscopy (SEM-EDS), and transmission electron microscopy (TEM).

XRD characterization was carried out in a STADI-P Stoe diffractometer, applying an angular scattering 2θ over 10 and 70°, step size of 2 °/min, and a monochromatic molybdenum energy source. The obtained results were analyzed in the X'pert HighScore Plus software and compared with the databank PDF-ICDD (International Crystallography Diffraction Databank). FE-SEM characterization was performed in FESEM JMS06701F (JEOL, Japan) microscope, using a 10 mm work distance and 10 kV voltage. SEM-EDS analysis was performed in an SEM JMS-6701F (JEOL, Japan) microscope in which the EDS mapping analysis was performed to detect Si, Ca, P, and Fe elements, applying a 10 kV voltage, and using a 12 mm work distance. (Dr. Muller, plese insert the TEM parameter here)

Magnetic Characterization: Curves of magnetization in the function of an applied magnetic field (M-H) were obtained in SQUID equipment (Quantum Design, USA), varying the magnetic field between -60 and 60 kOe, at room temperature (300 K). Field-cooling zero-field cooling (ZFC-FC) curves were obtained through cooling the samples until 2 K without the applied magnetic field. Then, a 500 Oe magnetic field was applied, and magnetization

measurements were collected, increasing the temperature from 2 K up to 300 K (ZFC curve). After this step, the samples were cooled again under the presence of a 500 Oe magnetic field (FC curve).

Calorimetric test: The ability of the nanocomposites to generate heat was estimated by means of an induction furnace (Egma 6, FELMI Srl, Italy) at 2 kW and 219 kHz. The temperature increase of a defined volume of water (2 ml) was evaluated up to 10 minutes using 20 mg of nanocomposite powder and the set up described in [ref]. The temperature variation was calculated by measuring the temperature before and after the heating by a digital thermocouple. All the measurements were reported as mean ± standard deviation.

Bioactivity test: Bioactivity test was performed using the simulated body fluid solution [5] prepared following the proposed literature. The liquid/powder ratio used in the test (1.5 mg/mL) followed the recommendation of the International Committee on Glass (ICG) for bioactivity test using powdered samples [61], and the experiment was carried out as previously reported by our research group [62]. In brief, 75 mg of glass or nanocomposite powder was placed in 50 mL of SBF solution in a polypropylene container. Then, the containers were shaken at 120 rpm for 1 and 7 days at physiological conditions (36.5 ± 0.5 ºC and pH 7.4). After each period, the powders were vacuum filtered, and the remaining solids were exhaustively rinsed with distilled water, alcohol, and acetone in order to wash SBF ionic residues and block further hydration reactions. Later, the powders were kept in a furnace at 37 °C for drying. Finally, the powders were characterized by XRD, SEM-EDS, and Fourier transform infrared spectroscopy (FTIR). In this experiment, the XRD analysis was performed in a D8 Focus diffractometer (Bruker AXS, USA), applying an angular scattering between 15 and 60°, step size of 1 °/min, and a monochromatic cupper energy font. The SEM-EDS analysis was carried out like previously reported.

The FTIR spectra were collected in a Varian AIM 8800 spectrometer over 450 and 4000 cm^{-1}, and using the transmission mode. The sample preparation was performed using a methodology described elsewhere [44], which allows the quantification of phosphate groups in the samples and, thereby, the bioactivity. Briefly, glass or nanocomposites (2.5 mg), iron (III) thiocyanate (5.7 mg), and potassium bromide (75 mg) were used to produce KBr window specimens. Also, a standard specimen was prepared by replacing glass by commercial hydroxyapatite (Sgima Aldrich, USA). The iron (III) thiocyanate was used as an internal standard, and all collected spectra were normalized regarding the C ≡ N (2121 cm^{-1}) functional group. Later, the areas below the peaks of $P{=}O_{cryst}$ (560 e 605 cm^{-1}) were quantified, which correspond to a typical crystalline calcium phosphate. The area of $P{=}O_{cryst}$ functional group from the hydroxyapatite sample (A_{HA}) was considered 100% hydroxyapatite, and the other specimens (A_{SBF}) were proportional to A_{HA}, as shown in Eq. 1:

$$(A_{SBF} \times 100)/A_{HA} = hydroxyapatite\ content\ in\ the\ sample\ (\%)$$

Dr. Emanuela and Dr. Marcia, please insert your methodologies here.

Supporting Information
Supporting information is available from the Wiley Online Library or from the author.

Acknowledgments

The authors acknowledge the facility support from the Universidade Federal do ABC, Central Experimental Multiusuário, Politecnico di Torino and Jena University. The authors also thank MSc. Marcela Tercini (Nano/UFABC) and BSc. João Francisco Almeida (CEM/UFABC) by the technical support in the FE-SEM analysis. Furthermore, the author appreciates the financial support from FAPESP (#2016/16512-9), FINEP, CNPq (#130637/2016-5), and CAPES (code 002).

Received: ((will be filled in by the editorial staff))
Revised: ((will be filled in by the editorial staff))
Published online: ((will be filled in by the editorial staff))

References

[1] A. Sohail, Z. Ahmad, O. A. Bég, S. Arshad, L. Sherin, *Bull. Cancer* **2017**, *104*, 452.

[2] M. Mikhaylova, D. K. Kim, N. Bobrysheva, M. Osmolowsky, V. Semenov, T. Tsakalakos, M. Muhammed, *Langmuir* **2004**, 2472.

[3] H. Wang, S. Zhao, J. Zhou, K. Zhu, Z. Cui, W. Huang, M. N. Rahaman, C. Zhang, D. Wang, *J. Mater. Chem. B* **2015**, 1.

[4] M. V Velasco, M. T. Souza, M. C. Crovace, A. J. A. De Oliveira, E. D. Zanotto, *Biomed. Glas.* **2019**, *5*, 148.

[5] T. Kokubo, H. Takadama, *Biomaterials* **2006**, *27*, 2907.

[6] L. L. Hench, *J. Mater. Sci. Mater. Med.* **2006**, *17*, 967.

[7] O. P. Filho, G. P. Latorre, L. L. Hench, *J. Biomed. Mater. Res. A* **1996**, *30*, 509.

[8] Y. Ebisawa, Y. Sugimoto, T. Hayashi, T. Kokubo, K. Ohura, T. Yamamuro, *Nippon Seramikkusu Kyokai Gakujutsu Ronbunshi* **1991**, *99*, 7.

[9] K. Ohura, M. Ikenaga, T. Nakamura, T. Yamamuro, *J. Appl. Biomater.* **1991**, *2*, 153.

[10] R. K. Singh, A. Srinivasan, *Appl. Surf. Sci.* **2010**, *256*, 1725.

[11] R. K. Singh, A. Srinivasan, *Ceram. Int.* **2010**, *36*, 283.

[12] R. K. Singh, A. Srinivasan, G. P. Kothiyal, *J. Mater. Sci. Mater. Med.* **2009**, *20*, 147.

[13] S. A. Shah, M. U. Hashmi, S. Alam, *Mater. Sci. Eng. C* **2011**, *31*, 1010.

[14] S. A. Shah, M. U. Hashmi, S. Alam, A. Shamim, *J. Magn. Magn. Mater.* **2010**, *322*, 375.

[15] G. Li, S. Feng, D. Zhou, *J. Mater. Sci. Mater. Med.* **2011**, *22*, 2197.

[16] R. Li, A. E. Clark, L. L. Hench, *J. Appl. Biomater.* **1991**, *2*, 231.

[17] P. Sepulveda, J. R. Jones, L. L. Hench, *J. Biomed. Mater. Res.* **2001**, 564.

[18] D. Arcos, R. P. Real, *J. Biomed. Mater. Res. A* **2003**, *65*, 71.

[19] G. Da, D. Li, Y. Lin, T. Hua, G. Sheng, Q. Dan, *Mater. Sci. Eng. C* **2010**, *30*, 148.

[20] E. Ruiz-Hernandez, M. C. Serrano, D. Arcos, M. Vallet-Regí, *J. Biomed. Mater. Res. A*

2006, *79*, 533.

[21] A. Matsumine, K. Takegami, K. Asanuma, T. Matsubara, *Int J Clin Oncol* **2011**, *16*, 101.

[22] X. Yan, C. Yu, X. Zhou, J. Tang, D. Zhao, *Angew. Chem. Int. Ed.* **2004**, *43*, 5980.

[23] X. X. Yan, H. X. Deng, X. H. Huang, G. Q. Lu, S. Z. Qiao, D. Y. Zhao, C. Z. Yu, *J. Non. Cryst. Solids* **2005**, *351*, 3209.

[24] C. Wu, W. Fan, Y. Zhu, M. Gelinsky, J. Chang, G. Cuniberti, V. Albrecht, T. Friis, Y. Xiao, *Acta Biomater.* **2011**, *7*, 3563.

[25] X. Li, X. Wang, Z. Hua, J. Shi, *Acta Mater.* **2008**, *56*, 3260.

[26] S. Kargozar, M. Mozafari, S. Hamzehlou, H. Kim, F. Baino, *Mater. Lett.* **2019**, *251*, 241.

[27] M. Baikousi, S. Agasthopoulos, I. Panagliotopoulos, A. D. Georgoulis, M. Louloudi, M. A. Karakassides, *J. Sol-Gel Sci. Technol.* **2008**, *47*, 95.

[28] B. E. Warren, J. Biscow, *J. Am. Ceram. Soc.* **1938**, *21*, 49.

[29] R. Frison, G. Cernuto, A. Cervellino, O. Zaharko, G. M. Colonna, A. Guagliardi, N. Masciocchi, *Chem. Mater.* **2013**, *25*, 4820.

[30] M. Cerruti, C. Morterra, *Langmuir* **2004**, *20*, 6382.

[31] S. Caldas, L. Silva, E. Araujo, *J. Non. Cryst. Solids* **2016**, *439*, 30.

[32] M. Mozafari, S. Banijamali, F. Baino, S. Kargozar, G. Hill, *Acta Biomater.* **2019**, DOI 10.1016/j.actbio.2019.04.039.

[33] L. A. Buchanan, A. El-ghannam, *J. Biomed. Mater. Res. A* **2009**, 538.

[34] W. Xia, J. Chang, *Mater. Lett.* **2007**, *61*, 3251.

[35] S. Lin, C. Ionescu, K. J. Pike, M. E. Smith, J. R. Jones, *J. Mater. Chem.* **2009**, *19*, 1276.

[36] G. Bihlmayer, *Handbook of Magnetism*, Jonh Wiley & Sons, **2007**.

[37] C. Cannas, G. Concas, D. Gatteschi, A. Falqui, A. Musinu, G. Piccaluga, C. Sangregorio, U. Cagliari, I. Nazionale, S. P. Monserrato, S. Km, I. M. Cagliari, U.

Firenze, V. Maragliano, I. Firenze, U. Cagliari, S. P. Monserrato, S. Km, I. M. Cagliari, *Phys. Chem. Chem. Phys.* **2001**, *3*, 832.

[38] T. Yang, C. Shen, Z. Li, H. Zhang, C. Xiao, S. Chen, Z. Xu, D. Shi, J. Li, H. Gao, *J. Phys. Chem. B* **2005**, *109*, 23233.

[39] K. Mandel, F. Hutter, C. Gellermann, G. Sextl, *J. Magn. Magn. Mater.* **2013**, *331*, 269.

[40] I. M. Lourenço, M. Pelegrino1, J. C. Pieretti1, G. P. Andrade, G. Cerchiaro, A. B. Seabra, *J. Phys. Conf. Ser.* **2019**, *1323*, 012015.

[41] Y. Deng, C. Wang, J. Hu, W. Yang, S. Fu, *Colloids Surfaces A Physicochem. Eng. Asp.* **2005**, *262*, 87.

[42] R. Borges, L. A. Genova, J. Marchi, in *Microspheres Technol. Appl. Role Drug Deliv. Syst.* (Eds.: D.R. de Araujo, L.R. Fraceto), Nova Publishers, **2014**.

[43] L. L. Hench, S. M. Best, in *Biomater. Sci. An Introd. to Mater. Med.* (Eds.: B.D. Ratner, A.S. Hoffman, F.. Schoen, J.E. Lemons), Academic Press, Oxford, **2013**.

[44] Y. Yu, Z. Bacsik, M. Eden, *Materials (Basel).* **2018**, *3*, 20.

[45] S. A. Macdonald, C. R. Schardt, D. J. Masiello, J. H. Simmons, *J. Non. Cryst. Solids* **2000**, *275*, 72.

[46] H. Aguiar, J. Serra, P. González, B. León, *J. Non. Cryst. Solids* **2009**, *355*, 475.

[47] J. Serra, P. González, S. Liste, S. Chiussi, B. León, M. Pérez-Amor, H. O. Ylänen, M. Hupa, *J. Mater. Sci. Mater. Med.* **2002**, *13*, 1221.

[48] I. Elgayar, A. E. Aliev, A. R. Boccaccini, R. G. Hill, *J. Non. Cryst. Solids* **2005**, *351*, 173.

[49] N. Shankhwar, A. Srinivasan, *Mater. Sci. Eng. C* **2016**, *62*, 190.

[50] A. Tilocca, A. N. Cormack, *ACS Appl. Mater. Interfaces* **2009**, *1*, 1324.

[51] R. K. Singh, A. Srinivasan, *J. Magn. Magn. Mater.* **2011**, *323*, 330.

[52] T. Leventouri, A. C. Kis, J. R. Thompson, I. M. Anderson, *Biomaterials* **2005**, *26*, 4924.

[53] O. Bretcanu, M. Miola, C. L. Bianchi, I. Marangi, R. Carbone, I. Corazzari, M. Cannas, E. Verné, *Mater. Sci. Eng. C* **2017**, *73*, 778.

[54] O. Bretcanu, S. Spriano, E. Verne, P. Tiberto, P. Allia, *Acta Biomater.* **2005**, *1*, 421.

[55] F. Baino, E. Fiume, M. Miola, F. Leone, B. Onida, E. Verné., *Mater Lett* **2019**, *235*, 207.

[56] T. G. Avancini, M. Tramontin, A. Pedro, N. De Oliveira, A. K. Alves, A. Pedro, N. De Oliveira, S. Arcaro, A. K. Alves, *Ceram. Int.* **2018**, DOI 10.1016/j.ceramint.2018.11.111.

[57] G. Li, K. Zhang, Z. Pei, N. Zhang, Y. Yu, S. Zhao, *Ceram. Int.* **2018**, *45*, 4945.

[58] T. Albrektsson, C. Johansson, *Eur. Spine J.* **2001**, *10*, 96.

[59] R. Borges, J. Marchi, *Adv. Sci. Technol.* **2016**, *102*, 18.

[60] E. Lee, J. Marchi, R. Borges, C. Eduardo, M. M. Marques, *Mater. Sci. Eng. C* **2018**, *Submitted*.

[61] A. L. B. Maçon, T. . Kim, E. M. Valliant, K. Goetschius, R. K. Brow, D. E. Day, A. Hoppe, A. R. Boccaccini, *J. Mater. Sci. Mater. Med.* **2015**, *25*, 115.

[62] T. Zambanini, R. Borges, P. C. Faria, G. P. Delpino, I. S. Pereira, M. M. Marques, J. Marchi, *Int. J. Appl. Ceram. Technol.* **2019**, *16*, 2028.

((Insert Figure here. Note: Please do not combine figure and caption in a textbox or frame.))
Figure 1. ((Figure Caption.))
Reproduced with permission.[Ref.] Copyright Year, Publisher. ((Permission statement required for all figures reproduced or adapted from previously published articles/sources; delete if not applicable))

Table 1. ((Table Caption. Note: Please do not combine table and caption in a textbox or frame and do not submit tables as graphics, please use Word's "insert table" function.))

Head 1 [units][a)]	Head 2	Head 3	Head 4	Head 5 [units]
Column 1	Column 2	Column 3[b)]	Column 4	Column 5
Column 1	Column 2	Column 3	Column 4	Column 5

[a)]((Table Footnote)); [b)] …

((**For Essays, Feature Articles, Progress Reports, and Reviews,** please insert up to three author biographies and photographs here, max. 100 words each))

Author Photograph(s) ((40 mm broad, 50 mm high, gray scale))

The table of contents entry should be 50–60 words long and should be written in the present tense and impersonal style (i.e., avoid we). The text should be different from the abstract text.

Keyword ((choose a broad keyword related to the research))

C. Author 2, D. E. F. Author 3, A. B. Corresponding Author* ((same order as byline))

Title ((no stars))

ToC figure ((Please choose one size: 55 mm broad × 50 mm high **or** 110 mm broad × 20 mm high. Please do not use any other dimensions))

((Supporting Information can be included here using this template))

Supporting Information

Title ((no stars))

*Author(s), and Corresponding Author(s)** ((write out full first and last names))

((Please insert your Supporting Information text/figures here. Please note: Supporting Display items, should be referred to as Figure S1, Equation S2, etc., in the main text…)